

ORIGINAL ARTICLE

Open Access



# Moderate active Fe<sup>3+</sup> doping enables improved cationic and anionic redox reactions for wide-voltage-range sodium storage

Congcong Cai<sup>1,2</sup>, Xinyuan Li<sup>2</sup>, Hao Fan<sup>2</sup>, Zhuo Chen<sup>2</sup>, Ting Zhu<sup>2</sup>, Jiantao Li<sup>4</sup>, Ruohan Yu<sup>2</sup>, Tianyi Li<sup>5</sup>, Ping Hu<sup>1,2,3\*</sup> and Liang Zhou<sup>1,2\*</sup>

## Abstract

Layered metal oxides are promising cathode materials for sodium-ion batteries (SIBs) due to their high theoretical specific capacity and wide Na<sup>+</sup> diffusion channels. However, the irreversible phase transitions and cationic/anionic redoxes cause fast capacity decay. Herein, P2-type Na<sub>0.67</sub>Mg<sub>0.1</sub>Mn<sub>0.8</sub>Fe<sub>0.1</sub>O<sub>2</sub> (NMMF-1) cathode material with moderate active Fe<sup>3+</sup> doping has been designed for sodium storage. Uneven Mn<sup>3+</sup>/Mn<sup>4+</sup> distribution is observed in NMMF-1 and the introduction of Fe<sup>3+</sup> is beneficial for reducing the Mn<sup>3+</sup> contents both at the surface and in the bulk to alleviate the Jahn–Teller effect. The moderate Fe<sup>3+</sup>/Fe<sup>4+</sup> redox can realize the best tradeoff between capacity and cyclability. Therefore, the NMMF-1 demonstrates a high capacity (174.7 mAh g<sup>-1</sup> at 20 mA g<sup>-1</sup>) and improved cyclability (78.5% over 100 cycles) in a wide-voltage range of 1.5–4.5 V (vs. Na<sup>+</sup>/Na). *In-situ* X-ray diffraction reveals a complete solid-solution reaction with a small volume change of 1.7% during charge/discharge processes and the charge compensation is disclosed in detail. This study will provide new insights into designing high-capacity and stable layered oxide cathode materials for SIBs.

**Keywords** Fe-doping, Wide-voltage-range, Solid solution reaction, Layered oxide, Sodium-ion batteries

## 1 Introduction

Sodium-ion batteries (SIBs) are considered as one of the most promising candidates for large-scale energy storage due to the abundant and low-cost sodium resources [1–5]. The cathode is a key component which largely

determines the cell performance [6]. The cathode materials for SIBs can be mainly divided into polyanionic compounds [7–10], Prussian blue and its analogues [11–13], and layered transition metal oxides [14–16]. Among them, the layered transition metal oxides are widely investigated for their high theoretical capacity, high tap density, and easy synthesis [17, 18].

Layered transition metal oxides (Na<sub>x</sub>TMO<sub>2</sub>, TM = transition metal) can be categorized into two main groups (P2- and O3-types) according to the sodium ion accommodating sites and the oxygen stacking sequences [19]. Compared with the O3-type Na<sub>x</sub>TMO<sub>2</sub>, the low-Na P2-type materials have many vacancies in Na layers and possess wide prismatic paths for sodium ion diffusion with a low diffusion barrier, which makes P2-type Na<sub>x</sub>TMO<sub>2</sub> a promising cathode material [20–22]. However, most P2-type Na<sub>x</sub>TMO<sub>2</sub> are generally stable in the potential range of 2–4.1 V (vs. Na<sup>+</sup>/Na) with low

\*Correspondence:

Ping Hu

huping316@163.com

Liang Zhou

liangzhou@whut.edu.cn

<sup>1</sup> Hubei Longzhong Laboratory, Wuhan University of Technology (Xiangyang Demonstration Zone), Xiangyang 441000, Hubei, China

<sup>2</sup> State Key Laboratory of Advanced Technology for Materials Synthesis and Processing, Wuhan University of Technology, Wuhan 430070, China

<sup>3</sup> School of Microelectronics, Hubei University, Wuhan 430062, PR China

<sup>4</sup> Chemical Sciences and Engineering Division, Argonne National Laboratory, Lemont, IL 60439, USA

<sup>5</sup> X-Ray Science Division, Argonne National Laboratory, 9700 South Cass Avenue, Lemont, IL 60439, USA



discharge capacities. With the widening of voltage range, the P2-type  $\text{Na}_x\text{TMO}_2$  is susceptible to phase transition (P2–O2/PO4) or irreversible oxygen redox, leading to drastic volume change and poor structural stability [23–25]. In addition, the existence of  $\text{Mn}^{3+}$  would present Jahn–Teller distortion, which lowers the  $\text{Na}^+$  mobility [26–28]. Although inactive element doping ( $\text{Mg}^{2+}$  [29, 30],  $\text{Al}^{3+}$  [31, 32],  $\text{Li}^+$  [33],  $\text{Zn}^{2+}$  [34], and  $\text{Ti}^{4+}$  [35, 36] etc.) have been proved to have a significant improvement in the structural stability of  $\text{Na}_x\text{TMO}_2$ . However, the inactive elements can't provide extra charge compensation, which decreases the theoretical capacities. Therefore, when considering the synthetic effect of introducing extra redoxes and stabilizing structure, the active elemental doping is an effect approach. For example, Wang et al. reported that the strong-electronegativity  $\text{Cu}^{2+}/\text{Cu}^{3+}$  redox can stabilize the Na-deficient P2- $\text{Na}_{2/3}\text{Mn}_{0.72}\text{Cu}_{0.22}\text{Mg}_{0.06}\text{O}_2$  phase to achieve reversible cationic and anionic redoxes [37]. Myung et al. developed the active  $\text{Ni}^{2+}$  doped P2- $\text{Na}_{0.75}[\text{Li}_{0.15}\text{Ni}_{0.15}\text{Mn}_{0.7}]\text{O}_2$  cathode material, and the active Ni doping not only decreases the voltage hysteresis but also improves the cycling stability [38]. From this point, searching for earth-abundant and moderate active element doping is urgently required.

Herein, we designed the P2- $\text{Na}_{0.67}\text{Mg}_{0.1}\text{Fe}_x\text{Mn}_{0.9-x}\text{O}_2$  ( $x=0, 0.1, 0.2$ ) cathode material with different contents of

active  $\text{Fe}^{3+}$  doping. Uneven distribution of  $\text{Mn}^{3+}/\text{Mn}^{4+}$  element is observed in  $\text{Na}_{0.67}\text{Mg}_{0.1}\text{Mn}_{0.8}\text{Fe}_{0.1}\text{O}_2$  (NMMF-1). It is demonstrated that introducing moderate  $\text{Fe}^{3+}$  can reduce the  $\text{Mn}^{3+}$  contents both at the surface and in the bulk to alleviate the Jahn–Teller effect. In-situ X-ray diffraction (XRD) characterization reveals that NMMF-1 exhibits a complete solid solution process in the wide voltage range of 1.5 – 4.5 V (vs.  $\text{Na}^+/\text{Na}$ ). It is also found that the moderate  $\text{Fe}^{3+}$  doping can introduce additional active  $\text{Fe}^{3+}/\text{Fe}^{4+}$  redox to realize a tradeoff between capacity and cyclability. Therefore, the NMMF-1 cathode material demonstrates a high capacity and improved cycling stability. This study will provide a new insight into constructing high capacity and stable layered metal oxide cathode materials for SIBs.

## 2 Results and discussion

A series of Fe-doped  $\text{Na}_{0.67}\text{Mg}_{0.1}\text{Mn}_{0.9-x}\text{Fe}_x\text{O}_2$  ( $x=0, 0.1, 0.2$ , NMMFs) are prepared by an organic acid-assisted solid-state reaction. The crystal structures of the as-prepared NMMFs are characterized by X-ray diffraction (XRD, Fig. S1). The Rietveld refinement patterns of  $\text{Na}_{0.67}\text{Mg}_{0.1}\text{Mn}_{0.9}\text{O}_2$  (NMM) and NMMF-1 are displayed in Fig. 1a–b. All NMMF samples can be well indexed to the P2-type layered structure with a space group of  $P63/mmc$ . According to the refinement results of NMM and

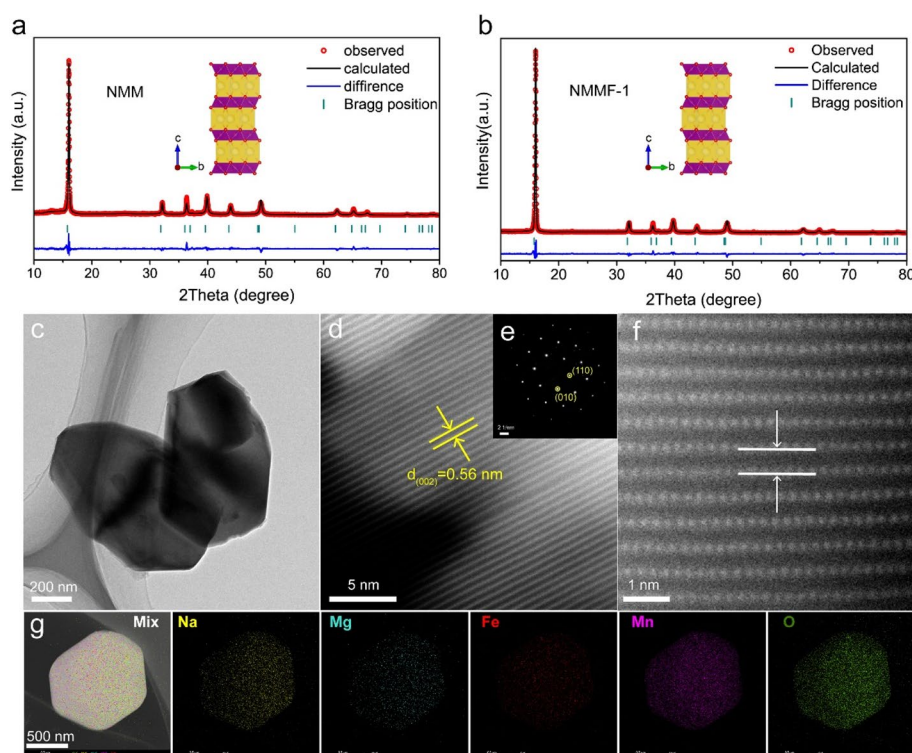


**Fig. 1** XRD Rietveld refinement patterns of (a) NMM and (b) NMMF-1, (c) TEM, (d, f) HRTEM, (e) SAED pattern, and (g) EDS-mappings of NMMF-1

NMMF-1 (Table S1-S2), both the Fe and Mg elements are contained in the TM layers. After introducing  $\text{Fe}^{3+}$  into NMM, the  $\text{Fe}^{3+}$  preferentially replaces the  $\text{Mn}^{3+}$  sites because of their same valence state (+3) and ionic radius (0.645 Å for  $\text{Fe}^{3+}$  and  $\text{Mn}^{3+}$ ), which is beneficial for alleviating the Jahn–Teller effect of  $\text{Mn}^{3+}$ .

The morphologies of the NMMFs are characterized by scanning electron microscopy (SEM) and transmission electron microscopy (TEM). SEM images (Fig. S2) indicate that all samples are composed of micro-particles with a size of 1–4 μm. The TEM image of NMMF-1 is displayed in Fig. 1c, where thick flakes can be observed. Figure 1d shows the high-resolution TEM (HRTEM) image of NMMF-1. Clear lattice fringes can be observed, corresponding to the (002) interplanar distance of P2 structure. Figure 1e shows the selected area electron diffraction (SAED) pattern along the  $[001]_{\text{hex}}$  zone axis. High-angle annular dark-field scanning transmission electron microscopy (HAADF-STEM) characterization is further employed to depict the atomic arrangement. The bright dots in Fig. 1f can be assigned to heavy TM atoms (Mn, Fe) and the light atoms can't be observed, which

reveals the typical layered structure of NMMF-1. The Energy dispersive spectroscopy (EDS) element mapping in Fig. 1g suggests that all elements are evenly distributed in NMMF-1.

As reported in many layered oxide cathode materials, the coexistence of  $\text{Mn}^{3+}$  and  $\text{Mn}^{4+}$  is a common phenomenon [27]. According to the chemical formula of NMMF-1, the average valence state of Mn is +3.54, suggesting the coexistence of  $\text{Mn}^{3+}$  and  $\text{Mn}^{4+}$ . To further investigate the distribution of  $\text{Mn}^{3+}$  and  $\text{Mn}^{4+}$  in the NMMF-1, HAADF-STEM coupled with electron energy loss spectroscopy (EELS) is employed (Fig. 2a). The bright fringes represent the heavy TM ions and the electron energy loss can be collected in EELS. The NMMF-1 is scanned from the surface to bulk with a length of 10 nm in linear scan mode, and the EELS spectra at different distances from the surface is shown in Fig. 2b, c. The EELS spectra of NMMF-1 display Mn-L3 and Mn-L2 peaks at ~644 and 654 eV, respectively, as well as the Fe-L3 peak at ~710 eV. It can be found that the Mn-L2,3 peaks shift to higher energy loss from surface to bulk with decreased intensity ratio of L3/L2, indicating the  $\text{Mn}^{3+}$  content is higher

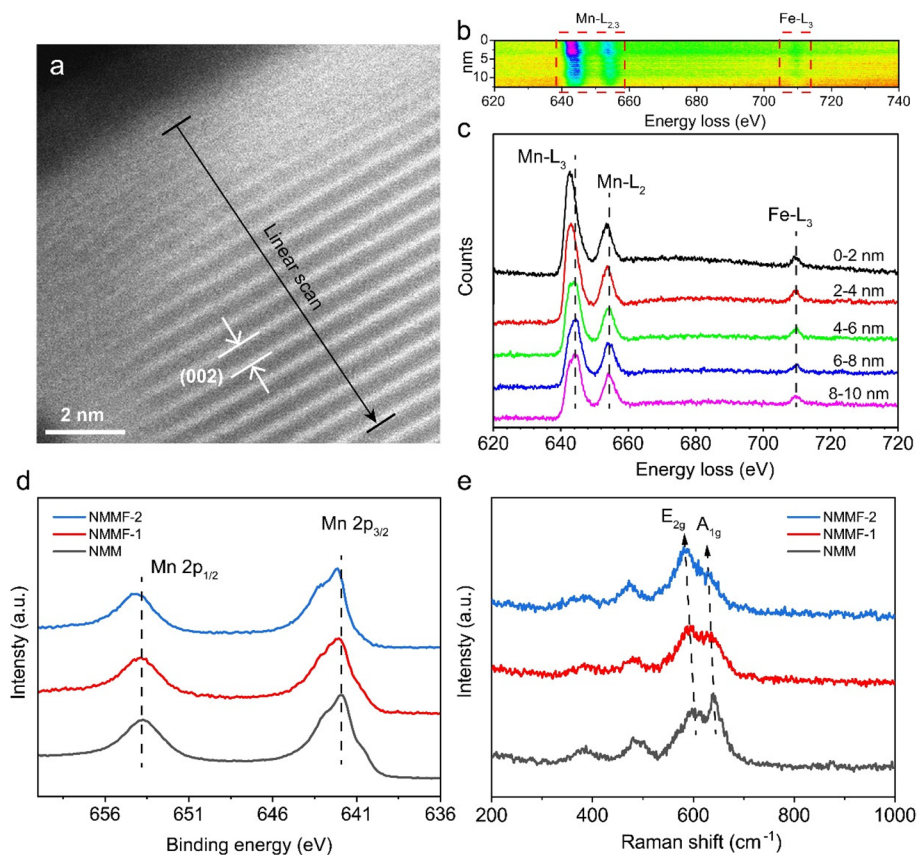


**Fig. 2** a HRTEM image of NMMF-1, (b-c) EELS counter pattern and spectra of NMMF-1, (d) XPS spectra and (e) Raman spectra of NMM, NMMF-1, and NMMF-2

at the edge [39]. The Fe-L3 peak shows no position and intensity change, which indicate the even distribution of  $\text{Fe}^{3+}$  at particle surface and bulk. Due to the similar ionic properties of  $\text{Fe}^{3+}$  and  $\text{Mn}^{3+}$ , the introduced  $\text{Fe}^{3+}$  should preferentially replaces  $\text{Mn}^{3+}$  sites. Thus, the introduced  $\text{Fe}^{3+}$  decreases the  $\text{Mn}^{3+}$  contents both at the surface and in the bulk. It is expected that the replacement of  $\text{Mn}^{3+}$  with  $\text{Fe}^{3+}$  would alleviate the Jahn–Teller distortion, thus leading to better material stability.

The integral valence states are investigated by XPS. The binding energies at 720 and 706 eV (Fig. S5) are corresponding to the Fe  $2p_{1/2}$  and  $2p_{3/2}$  peaks of  $\text{Fe}^{3+}$ , respectively. The peak intensity of  $\text{Fe}^{3+}$  increases from NMM to NMMF-2. The peaks show no shift in position, confirming the introduced iron keeps trivalent. Besides, the XPS spectra (Fig. 2d) display the Mn  $2p_{1/2}$  and  $2p_{3/2}$  peaks at  $\sim 653.8$  and  $\sim 642.0$  eV, respectively. The peaks gradually shift to higher binding energy from NMM to NMMF-2, indicating the increasing of Mn average valence state due to the substitution of  $\text{Mn}^{3+}$  by  $\text{Fe}^{3+}$ .

To further detect the change of local structures, Raman tests also are performed (Fig. 2e). All the samples exhibit four primary peaks, where the peak at  $640\text{ cm}^{-1}$  is assigned to the  $A_{1g}$  mode of TM–O bond and the peaks at  $\sim 598$ ,  $\sim 490$ , and  $\sim 380\text{ cm}^{-1}$  are ascribed to  $E_{2g}$  modes involving both Na and O vibrations [40, 41]. Typically, the  $E_{2g}$  peak at  $\sim 598\text{ cm}^{-1}$  is related to the atomic displacement along  $c$  axis, which is able to reflect the change in interlayer distance. Notably, with the increase

of introduced  $\text{Fe}^{3+}$  contents, the peak of  $A_{1g}$  mode shifts to lower position, which suggests the elongated TM–O bonds. The increased TM–O bonds are beneficial to increasing the structural stability. While the  $E_{2g}$  mode at  $\sim 598\text{ cm}^{-1}$  also shifts to lower wavenumbers, which suggests the increased interlayer distance.

The electrochemical performances of NMMFs are investigated in half cell with Na metal as the anode. The first two CV curves at  $0.1\text{ mV s}^{-1}$  of NMMF-1 are displayed in Fig. 3a. The NMMF-1 exhibits a pair of redox peaks below 2.5 V, which can be assigned to the oxidation/reduction of  $\text{Mn}^{3+}/\text{Mn}^{4+}$ . In addition, a sharp oxidation peak appears above 4.2 V, which generally corresponds to the anionic redox reaction and electrolyte decomposition. The peak exhibits a slight decrease at the second cycle, implying the existing of some irreversible processes. A small pair of peaks can also be observed within 3.5–4 V for NMMF-1, which may be ascribed to the redox of  $\text{Fe}^{3+}/\text{Fe}^{4+}$ . To further investigate the cycling stability, the NMMFs are tested at  $20\text{ mA g}^{-1}$  in a wide voltage range of 1.5–4.5 V, which involves both the cationic and anionic redoxes. The charge/discharge profiles of NMMF-1 at different cycles are shown in Fig. 3b. An obvious potential plateau at  $\sim 2\text{ V}$  is assigned to the  $\text{Mn}^{3+}/\text{Mn}^{4+}$  redox, agreeing with the CV results. The discharge profiles exhibit a good overlap during subsequent cycles, indicating the good reversibility. However, the NMM and NMMF-2 (Fig. S6) exhibit severe voltage decay during cycling. The cycling performances of NMMFs

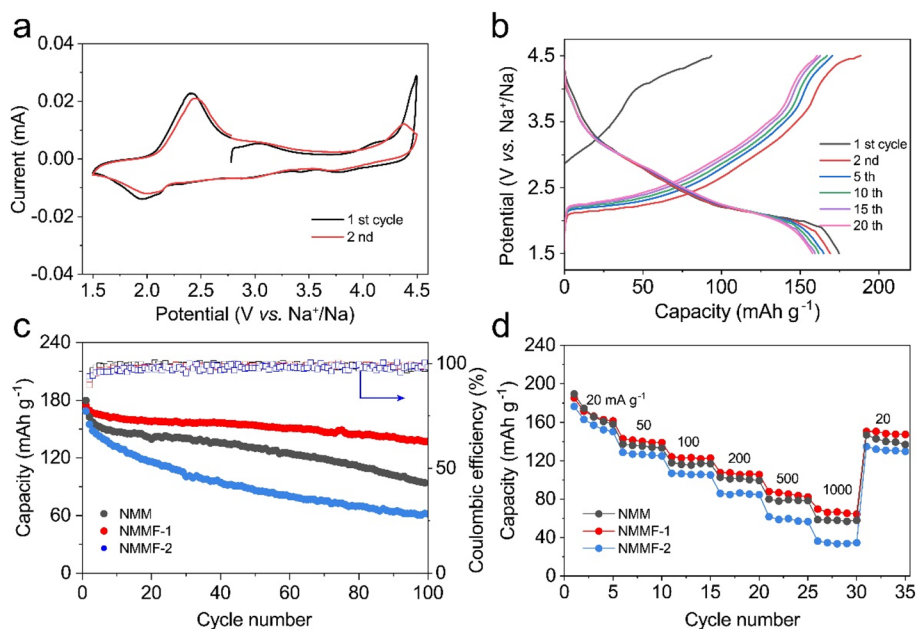


**Fig. 3** a CV curves and (b) charge/discharge profiles of NMMF-1, (c) cycling performances and (d) rate performances of NMM, NMMF-1, and NMMF-2

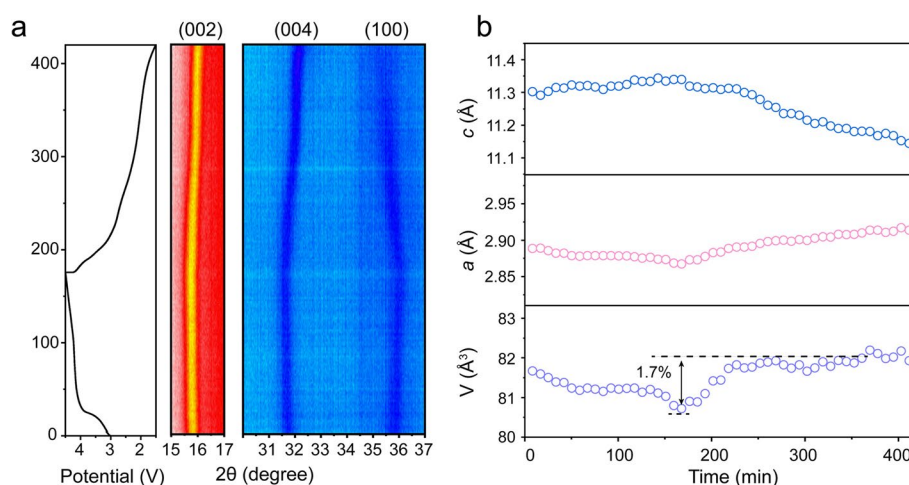


**Fig. 4** a In-situ XRD patterns of NMMF-1, (b) lattice parameter variation during charging/discharging processes

are investigated in 1.5–4.5 V (Fig. 3c). When tested at 20 mA g<sup>-1</sup>, the NMMF-1 delivered a high capacity of 174.7 mAh g<sup>-1</sup>, higher than that of NMMF-2 (168.6 mAh g<sup>-1</sup>) but slightly lower than NMM (179.5 mAh g<sup>-1</sup>). The slightly higher capacity of NMM may be related to the more Mn–O bonds, which are easier to trigger anionic redox reactions. After 100 cycles, the NMMF-1 exhibits significantly improved capacity retention of 78.5%, obviously higher than that of NMM (51.7%) and NMMF-2 (36.5%). The results indicate that the moderate active Fe<sup>3+</sup> doping improves the cycling stability. The rate performances of NMMFs are further tested (Fig. 3d, Fig. S8). The NMMF-1 also delivers higher capacity than NMM and NMMF-2 at different current densities. Even tested at the current density of 1000 mA g<sup>-1</sup>, the NMMF-1 can still deliver a high capacity of 69.8 mAh g<sup>-1</sup>.

The Galvanostatic intermittent titration technique (GITT) test at the second cycle is employed to compare the Na<sup>+</sup> diffusion coefficient ( $D_{Na^+}$ ) in NMM and NMMF-1 (Fig. S9). At the initial charge state, NMMF-1 exhibits a slightly higher Na<sup>+</sup> diffusion coefficient ( $D_{Na^+}$ ) than NMM, which explains the slight improvement of rate performance.

To explore the structural evolution of NMMF-1 during sodiation/de-sodiation processes, in-situ XRD measurements are employed. As displayed in Fig. 4a, during the charge process, the (002) and (004) peaks of NMMF-1 shift to lower position, which is related to the increase of lattice parameter  $c$  with the extraction of Na<sup>+</sup> ions. In contrast, the (100) peak shifts to higher position, indicating the decrease of lattice parameter  $a$ . As for the subsequent discharge process, the peak shifting shows an opposite behavior, indicating the reversible structure evolution. There are no new peaks appearing during the

whole charge/discharge processes, indicating a complete solid solution process, which demonstrates the stable structure of NMMF-1 within a wide voltage range of 1.5–4.5 V. The specific numerical changes in lattice parameters of NMMF-1 are displayed in Fig. 4b. The increase of parameter  $c$  is caused by the increased repulsive force between adjacent oxygen layers with the extraction of Na<sup>+</sup> ions. The decrease of parameter  $a$  can be ascribed to the TM oxidation, which makes TM–O distance shorter. Typically, NMMF-1 exhibits a low cell volume variation of 1.7%, suggesting a near-zero-strain feature.

To further clarify the charge compensation mechanism in NMMF-1, ex-situ X-ray adsorption near edge structure (XANES) at different charge/discharge states are collected. The normalized Fe K-edge and Mn K-edge spectra of the pristine and the charged states are displayed in Fig. 5a–b. The Fe K-edge exhibits a shift to high energy after fully charging, which manifests the oxidation of Fe<sup>3+</sup> to Fe<sup>4+</sup> in charge compensation process. The Mn K-edge spectra also slightly shifts to high energy from the pristine state to charged state, indicating the oxidation of Mn<sup>3+</sup> to Mn<sup>4+</sup>. The ex-situ O 1s XPS are further employed to detect the existence of oxygen redox reactions (Fig. 5c). The pristine O1s spectra can be divided into two peaks from the surface oxygen-related species and one peak from lattice oxygen. When charged to 4.5 V, an extra peak at 531 eV appears and disappears after fully discharged to 1.5 V, which is ascribed to the formation of peroxo-like (O<sub>2</sub>)<sup>n-</sup> species [42]. Such an appearance of the new component indicates the participation of the oxygen redox in charge compensation process. Because of the similar oxidizing potential of Fe<sup>3+</sup>/Fe<sup>4+</sup> and oxygen redox, the NMMF-2 with high-content Fe<sup>3+</sup> may experience simultaneously proceeding of cationic and anionic

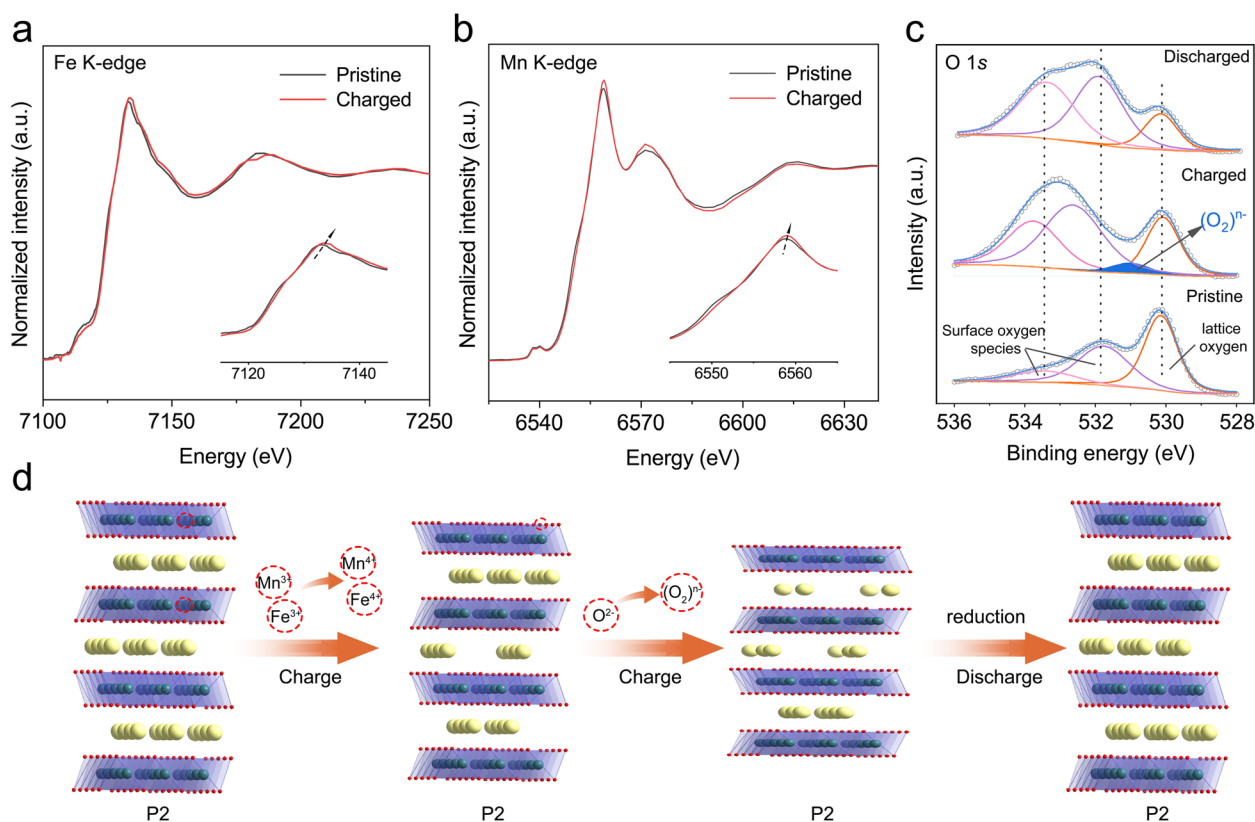


**Fig. 5** Ex-situ XANES spectra of (a) Fe K-edge and (b) Mn K-edge spectra, (c) ex-situ O 1s XPS spectra of NMMF-1. **d** Schematical illustration of the sodium storage processes of NMMF-1

redoxes and severely deteriorate the structure. Therefore, the entire charge compensation process of NMMF-1 can be schematically illustrated in Fig. 5d. The NMMF-1 cathode material exhibits a complete solid-solution reaction during the entire charge/discharge processes due to the  $\text{Mg}^{2+}$  and moderate  $\text{Fe}^{3+}$  dual doping,  $\text{Mg}^{2+}$  doping suppresses the unamiable phase transformation and triggers the anionic redox reactions, while  $\text{Fe}^{3+}$  doping is beneficial to reducing  $\text{Mn}^{3+}$  contents. In addition, the  $\text{Fe}^{3+}$  can be oxidized to  $\text{Fe}^{4+}$  to form strong Fe–O bonds, which would improve the anionic redox reversibility at high voltage. During the charge process, the capacity is provided by the cationic ( $\text{Fe}^{3+}/\text{Fe}^{4+}$ ,  $\text{Mn}^{3+}/\text{Mn}^{4+}$ ) and anionic ( $\text{O}^{2-}/(\text{O}_2)^{n-}$ ) redoxes. Due to the abundant redox reactions, NMMF-1 delivers a high capacity. The stable P2 structures of NMMF-1 at different charge states ensures the reversibility of these cationic/anionic redoxes.

### 3 Conclusion

In summary, we designed the  $\text{P2-Na}_{0.67}\text{Mg}_{0.1}\text{Mn}_{0.9-x}\text{Fe}_x\text{O}_2$  ( $x=0, 0.1, 0.2$ ) cathode material with different contents of active  $\text{Fe}^{3+}$  doping. The uneven  $\text{Mn}^{3+}/\text{Mn}^{4+}$  distribution is observed in  $\text{Na}_{0.67}\text{Mg}_{0.1}\text{Fe}_{0.1}\text{Mn}_{0.8}\text{O}_2$  (NMMF-1). It is demonstrated that introducing moderate  $\text{Fe}^{3+}$  can reduce the  $\text{Mn}^{3+}$  contents both at the surface and in the bulk to alleviate the Jahn–Teller effect. The structural evolution and charge compensation mechanism are revealed by in-situ XRD and ex-situ XANES/XPS measurements. The NMMF-1 exhibits a complete solid-solution reaction during the entire charge/discharge processes. What's more, it is found that the introduction of  $\text{Fe}^{3+}$  can bring in additional active  $\text{Fe}^{3+}/\text{Fe}^{4+}$  redox, the moderate  $\text{Fe}^{3+}$  doping can realize a tradeoff between capacity and cyclability. Therefore, the NMMF-1 cathode material exhibits a high capacity and improved cycling stability in a wide-voltage range of 1.5–4.5 V (V vs.  $\text{Na}^+/\text{Na}$ ). This study will provide a new insight into constructing high capacity and stable cathode for SIBs.

## Abbreviations

|                           |   |
|---------------------------|---|
| SIBs                      | Sodium-ion batteries  |
| LIBs                      | Lithium-ion batteries   |
| $\text{Na}_x\text{TMO}_2$ | Layered transition metal oxides   |
| NMM                       | $\text{Na}_{0.67}\text{Mg}_{0.1}\text{Mn}_{0.9}\text{O}_2$                |
| NMMF-1                    | $\text{Na}_{0.67}\text{Mg}_{0.1}\text{Mn}_{0.8}\text{Fe}_{0.1}\text{O}_2$ |
| NMMF-2                    | $\text{Na}_{0.67}\text{Mg}_{0.1}\text{Mn}_{0.7}\text{Fe}_{0.2}\text{O}_2$ |

## Supplementary Information

The online version contains supplementary material available at <https://doi.org/10.1007/s43979-023-00077-1>.

### Additional file 1.

## Acknowledgements

The STEM was performed at the Nanostructure Research Center (NRC). This research used resources of the Advanced Photon Source, a U.S. Department of Energy (DOE) Office of Science User Facility, operated for the DOE Office of Science by Argonne National Laboratory under Contract No. DE-AC02-06CH11357.

## Authors' contributions

CC was in charge of the experimental design and analysis, synthesis and characterization of the samples, and original draft writing. XL and HF conceived the idea and assisted with characterizations; ZC and TZ reviewed and revised the manuscript; JL and TL performed the XANES characterization; RY performed the HRTEM characterization; PH and LZ administrated the project, supervised the experiments, wrote and revised the draft, and raised funding. The final version of the paper has been approved by all authors.

## Funding

This work was supported by the National Natural Science Foundation of China (U23A20684) and Independent Innovation Project of Hubei Longzhong Laboratory (2022ZZ-18).

## Availability of data and materials

The data and materials are available upon reasonable request.

## Declarations

### Ethics approval and consent to participate

All authors have seen the manuscript and approved to submit to the journal.

### Consent for publication

This manuscript has not been published in whole or in part nor is it being considered for publication elsewhere.

### Competing interests

There are no financial interests that are directly or indirectly related to the work submitted for publication.

Received: 3 August 2023 Revised: 7 November 2023 Accepted: 19 December 2023

Published online: 09 January 2024

## References

- Hwang JY, Myung ST, Sun YK (2017) Sodium-ion batteries: present and future. *Chem Soc Rev* 46(12):3529–3614
- Chen S, Wu C, Shen L, Zhu C, Huang Y, Xi K, Maier J, Yu Y (2017) Challenges and perspectives for NASICON-type electrode materials for advanced sodium-ion batteries. *Adv Mater* 29(48):1700431
- Zhao C, Wang Q, Yao Z, Wang J, Sánchez-Lengeling B, Ding F, Qi X, Lu Y, Bai X, Li B, Li H, Aspuru-Guzik A, Huang X, Delmas C, Wagemaker M, Chen L, Hu Y-S (2020) Rational design of layered oxide materials for sodium-ion batteries. *Science* 370(6517):708–711
- Zhang Q, Lu Y, Guo W, Shao Y, Liu L, Lu J, Rong X, Han X, Li H, Chen L, Hu Y-S (2021) Hunting sodium dendrites in NASICON-based solid-state electrolytes. *Energy Mater Adv* 2021:9870879
- Zhu N, Zhang K, Wu F, Bai Y, Wu C (2021) Ionic liquid-based electrolytes for aluminum/magnesium/sodium-ion batteries. *Energy Material Adv* 2021:9204217
- Li Y, Zheng Y, Guo K, Zhao J, Li C (2022) Mg-Li hybrid batteries: the combination of fast kinetics and reduced overpotential. *Energy Material Adv* 2022:9840837
- Zhu T, Hu P, Cai C, Liu Z, Hu G, Kuang Q, Mai L, Zhou L (2020) Dual carbon decorated  $\text{Na}_3\text{MnTi}(\text{PO}_4)_3$ : a high-energy-density cathode material for sodium-ion batteries. *Nano Energy* 70:104548
- Jin T, Li H, Zhu K, Wang PF, Liu P, Jiao L (2020) Polyanion-type cathode materials for sodium-ion batteries. *Chem Soc Rev* 49(8):2342–2377
- Gezović A, Vujković MJ, Milović M, Grudić V, Dominko R, Mentus S (2021) Recent developments of  $\text{Na}_4\text{M}_3(\text{PO}_4)_2(\text{P}_2\text{O}_7)$  as the cathode material for alkaline-ion rechargeable batteries: challenges and outlook. *Energy Storage Mater* 37:243–273
- Zhang Q, Shen X, Zhou Q, Li K, Ding F, Lu Y, Zhao J, Chen L, Hu Y-S (2022) Large scale one-pot synthesis of monodispersed  $\text{Na}_3(\text{VOPO}_4)_2\text{F}$  cathode for na-ion batteries. *Energy Mater Adv* 2022:9828020
- Zhou A, Cheng W, Wang W, Zhao Q, Xie J, Zhang W, Gao H, Xue L, Li J (2020) Hexacyanoferrate-Type Prussian blue analogs: principles and advances toward high-performance sodium and potassium ion batteries. *Adv Energy Mater* 11(2):2000943
- Peng J, Zhang W, Liu Q, Wang J, Chou S, Liu H, Dou S (2022) Prussian blue analogues for sodium-ion batteries: past, present, and future. *Adv Mater* 34(15):2108384
- Peng J, Ou M, Yi H, Sun X, Zhang Y, Zhang B, Ding Y, et al (2021) Defect-free-induced  $\text{Na}^+$  disordering in electrode materials. *Energy Environ Sci* 14(5):3130–3140
- Ding F, Zhao C, Xiao D, Rong X, Wang H, Li Y, Yang Y, Lu Y, Hu YS (2022) Using high-entropy configuration strategy to design na-ion layered oxide cathodes with superior electrochemical performance and thermal stability. *J Am Chem Soc* 144(18):8286–8295
- Ding F, Zhao C, Zhou D, Meng Q, Xiao D, Zhang Q, Niu Y, Li Y, Rong X, Lu Y, Hu CLYS (2020) A novel Ni-rich  $\text{O}_3\text{-Na}[\text{Ni}_{0.60}\text{Fe}_{0.25}\text{Mn}_{0.15}]\text{O}_2$  cathode for Na-ion batteries. *Energy Storage Mater* 30:420–430
- Fu F, Liu X, Fu X, Chen H, Huang L, Fan J, Le J, Wang Q, Yang W, Ren Y, Amine K, Sun SG, Xu GL (2022) Entropy and crystal-facet modulation of P2-type layered cathodes for long-lasting sodium-based batteries. *Nat Commun* 13(1):2826
- Liu Q, Hu Z, Li W, Zou C, Jin H, Wang S, Chou S, Dou S-X (2021) Sodium transition metal oxides: the preferred cathode choice for future sodium-ion batteries? *Energy Environ Sci* 14(1):158–179
- Han MH, Gonzalo E, Singh G, Rojo T (2015) A comprehensive review of sodium layered oxides: powerful cathodes for Na-ion batteries. *Energy Environ Sci* 8(1):81–102
- Yabuuchi N, Kubota K, Dahbi M, Komaba S (2014) Research development on sodium-ion batteries. *Chem Rev* 114(23):11636–11682
- Wang P-F, Yao H-R, Liu X-Y, Yin Y-X, Zhang J-N, Wen Y, Yu X, Gu L (2018) Guo Y-G  $\text{Na}^+$ /vacancy disordering promises high-rate Na-ion batteries. *Sci Adv* 4(3):eaar6018
- Wang S, Sun C, Wang N, Zhang Q (2019) Ni- and/or Mn-based layered transition metal oxides as cathode materials for sodium ion batteries: status, challenges and countermeasures. *J Mater Chem A* 7(17):10138–10158
- Peng B, Wan G, Ahmad N, Yu L, Ma X, Zhang G (2023) Recent progress in the emerging modification strategies for layered oxide cathodes toward practicable sodium ion batteries. *Adv Energy Mater* 13(27):2300334
- Somerville JW, Sobkowiak A, Tapia-Ruiz N, Billaud J, Lozano JG, House RA, Gallington LC, Ericsson T, Häggström L, Roberts MR, Maitra U, Bruce PG (2019) Nature of the “Z”-phase in layered Na-ion battery cathodes. *Energy Environ Sci* 12(7):2223–2232
- Jin T, Wang PF, Wang QC, Zhu K, Deng T, Zhang J, Zhang W, Yang XQ, Jiao L, Wang C (2020) Realizing complete solid-solution reaction in high sodium content P2-type cathode for high-performance sodium-ion batteries. *Angew Chem Int ed* 59(34):14511–14516
- Xu H, Guo S, Zhou H (2019) Review on anionic redox in sodium-ion batteries. *J Mater Chem A* 7(41):23662–23678

26. Zheng L, Wang Z, Wu M, Xu B, Ouyang C (2019) Jahn-Teller type small polaron assisted Na diffusion in NaMnO<sub>2</sub> as a cathode material for Na-ion batteries. *J Mater Chem A* 7(11):6053–6061
27. Kumakura S, Tahara Y, Kubota K, Chihara K, Komaba S (2016) Sodium and Manganese stoichiometry of P2-type Na<sub>2/3</sub>MnO<sub>2</sub>. *Angew Chem Int Ed* 55(41):12760–12763
28. Zhao S, Shi Q, Feng W, Liu Y, Yang X, Zou X, Lu X, Zhao Y (2023) Research progresses in O3-type Ni/Fe/Mn based layered cathode materials for sodium ion batteries. *Carbon Neutrality* 2(1):13
29. Wang PF, You Y, Yin YX, Wang YS, Wan LJ, Gu L, Guo YG (2016) Suppressing the P2-O2 Phase Transition of Na<sub>0.67</sub>Mn<sub>0.67</sub>Ni<sub>0.33</sub>O<sub>2</sub> by Magnesium substitution for improved sodium-ion batteries. *Angew Chem Int Ed* 55(26):7445–7449
30. Huang Y, Zhu Y, Nie A, Fu H, Hu Z, Sun X, Haw S-C, Chen J-M, Chan T-S, Yu S, Sun G, Jiang G, Han J, Luo W, Huang Y (2022) Enabling anionic redox stability of P2-Na<sub>5/6</sub>Li<sub>1/4</sub>Mn<sub>3/4</sub>O<sub>2</sub> by Mg substitution. *Adv Mater* 34(9):2105404
31. Liu X, Zuo W, Zheng B, Xiang Y, Zhou K, Xiao Z, Shan P, Shi J, Li Q, Zhong G, Fu R, Yang Y (2019) P2-Na<sub>0.67</sub>Al<sub>x</sub>Mn<sub>1-x</sub>O<sub>2</sub>: Cost-effective, stable and high-rate sodium electrodes by suppressing phase transitions and enhancing sodium cation mobility. *Angew Chem Int Ed* 58(50):18086–18095
32. Cai C, Li X, Hu P, Zhu T, Li J, Fan H, Yu R, Zhang T, Lee S, Zhou L, Mai L (2023) Comprehensively strengthened metal-oxygen bonds for reversible anionic redox reaction. *Adv Funct Mater* 33(24):2215155
33. Yang L, Li X, Liu J, Xiong S, Ma X, Liu P, Bai J, Xu W, Tang Y, Hu YY, Liu M, Chen H (2019) Lithium-doping stabilized high-performance P2-Na<sub>0.66</sub>Li<sub>0.18</sub>Fe<sub>0.12</sub>Mn<sub>0.7</sub>O<sub>2</sub> cathode for sodium ion batteries. *J Am Chem Soc* 141(16):6680–6689
34. Wang Y, Wang L, Zhu H, Chu J, Fang Y, Wu L, Huang L, Ren Y, Sun CJ, Liu Q, Ai X, Yang H, Cao Y (2020) Ultralow-strain Zn-substituted layered oxide cathode with suppressed P2–O2 transition for Stable sodium ion storage. *Adv Funct Mater* 30(13):1910327
35. Cao X, Li X, Qiao Y, Jia M, Qiu F, He Y, He P, Zhou H (2019) Restraining oxygen loss and suppressing structural distortion in a newly Ti-substituted layered oxide P2-Na<sub>0.66</sub>Li<sub>0.22</sub>Ti<sub>0.15</sub>Mn<sub>0.63</sub>O<sub>2</sub>. *ACS Energy Lett* 4(10):2409–2417
36. Sato T, Yoshikawa K, Zhao W, Kobayashi T, Rajendra HB, Yonemura M, Yabuuchi N (2021) Efficient stabilization of Na storage reversibility by Ti integration into O'3-Type NaMnO<sub>2</sub>. *Energy Mater Adv* 2021:9857563
37. Wang P-F, Xiao Y, Piao N, Wang Q-C, Ji X, Jin T, Guo Y-J, Liu S, Deng T, Cui C, Chen L, Guo Y-G, Yang X-Q, Wang C (2020) Both cationic and anionic redox chemistry in a P2-type sodium layered oxide. *Nano Energy* 69:104474
38. Voronina N, Shin MY, Kim HJ, Yaqoob N, Guillon O, Song SH, Kim H, Lim HD, Jung HG, Kim Y, Lee HK, Lee KS, Yazawa K, Gotoh K, Kaghazchi P, Myung ST (2022) Hysteresis-suppressed reversible oxygen-redox cathodes for sodium-ion batteries. *Adv Energy Mater* 12(21):2103939
39. Ma C, Alvarado J, Xu J, Clement RJ, Kodur M, Tong W, Grey CP, Meng YS (2017) Exploring oxygen activity in the high energy P2-Type Na<sub>0.78</sub>Ni<sub>0.23</sub>Mn<sub>0.69</sub>O<sub>2</sub> cathode material for na-ion batteries. *J Am Chem Soc* 139(13):4835–4845
40. Singh G, López del Amo JM, Galceran M, Pérez-Villar S, Rojo T (2015) Structural evolution during sodium deintercalation/intercalation in Na<sub>2/3</sub>[Fe<sub>1/2</sub>Mn<sub>1/2</sub>]O<sub>2</sub>. *J Mater Chem A* 3(13):6954–6961
41. Shi YG, Liu YL, Yang HX, Nie CJ, Jin R, Li JQ (2004) Raman spectroscopy study of Na<sub>x</sub>CoO<sub>2</sub> and superconducting Na<sub>x</sub>CoO<sub>2</sub>·yH<sub>2</sub>O. *Phys Rev B* 70(5):052502
42. Yoon GH, Koo S, Park SJ, Lee J, Koo C, Song SH, Jeon TY, Kim H, Bae JS, Moon WJ, Cho SP, Kim D, Yu SH (2022) Enabling stable and nonhysteretic oxygen redox capacity in Li-excess Na layered oxides. *Adv Energy Mater* 12(11):2103384

## Publisher's Note

Springer Nature remains neutral with regard to jurisdictional claims in published maps and institutional affiliations.